Weak and strong hydrogen bonds conducting the supramolecular framework of 1-butyl-3-(1-naphthoyl)thiourea: crystal structure, vibrational studies, DFT methods, Pixel energies and Hirshfeld surface analysis

E. Contreras Aguilar, G. A. Echeverría, O. E. Piro, S. E. Ulic, J. L. Jios, M. E. Tuttolomondo & H. Pérez

View supplementary material

Published online: 10 Nov 2017.

Submit your article to this journal

View related articles

View Crossmark data

Taylor & Francis
Taylor & Francis Group

RESEARCH ARTICLE

Check for updates

Weak and strong hydrogen bonds conducting the supramolecular framework of 1-butyl-3-(1-naphthoyl)thiourea: crystal structure, vibrational studies, DFT methods, Pixel energies and Hirshfeld surface analysis

E. Contreras Aguilar[a], G. A. Echeverría[b], O. E. Piro[b], S. E. Ulic[a,c], J. L. Jios[d], M. E. Tuttolomondo[e] and H. Pérez[f]

[a]CEQUINOR (CONICET-UNLP), Facultad de Ciencias Exactas, Universidad Nacional De La Plata, La Plata, República Argentina; [b]Departamento De Física, Facultad de Ciencias Exactas, Universidad Nacional De La Plata e IFLP (CONICET, CCT-La Plata), La Plata, República Argentina; [c]Departamento De Ciencias Básicas, Universidad Nacional De Luján, Luján, Buenos Aires, República Argentina; [d]UNIDAD PLAPIMU-LASEISIC (UNLP-CIC), Departamento de Química, Facultad de Ciencias Exactas, Universidad Nacional De La Plata, La Plata, República Argentina; [e]INQUINOA, CONICET – Instituto de Química Física, Facultad de Bioquímica, Química y Farmacia, Universidad Nacional De Tucumán, Tucumán, Argentina; [f]Departamento De Química General e Inorgánica, Facultad de Química, Universidad de La Habana, La Habana, Cuba
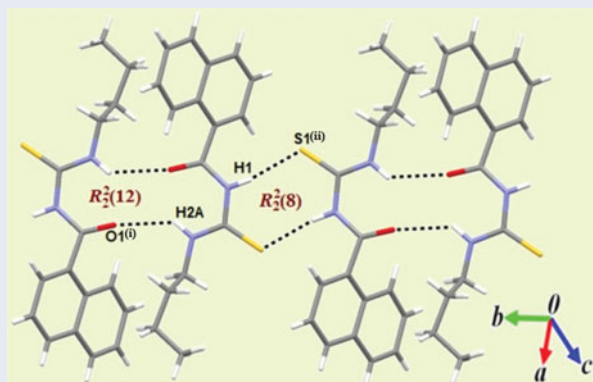
ABSTRACT

A detailed structural and spectroscopic study of a new thiourea derivative 1-butyl-3-(1-naphthoyl)thiourea (**1**) is presented with the assistance of theoretical calculations. The X-ray diffraction structure analysis reveals a planar carbonylthiourea group, favoured by intra-molecular NH···O bond. The compound is arranged in the lattice as NH···O and NH···S bonded polymeric ribbons, that extend along the crystal b-axis. Molecular pairs involving N–H···S hydrogen bonds are a dominant contribution to packing stabilisation coming from coulombic component. Hirshfeld surfaces and two-dimensional-fingerprint plots show different intermolecular contacts and its relative contributions to total surface in each compound. The AIM approach shows the nature and strength of the strong and weak intramolecular interactions and the solvent effect, while NBO analysis reveals that the sulphur atom is responsible for the higher hyperconjugative stabilising energy.

1. Introduction

Arylthiourea derivatives have shown activity against Hepatitis C virus (HCV) infection [1], and against pathogenic fungi [2]. Related aroylthioureas (Ar-CO-NH-CS-NRR') were tested against three parasites of human relevance, colon cancer cells and human foreskin fibroblasts [3], and were found to be potent inhibitors of urease [4]. They act as co-ligands in Pd(II) complexes showing liquid crystal properties [5] and have been used extensively for the extraction of metals due to their strong coordination ability to form metallated complexes [6] such as in the solvent extraction of copper(II) [7] and palladium(II) and gold(III) [8] from aqueous chloride media. These compounds are also used as carriers from membrane transport of gold(III) across a polymer-immobilised liquid membrane [9]. Theoretical study of compounds with potential bioactivity is a useful
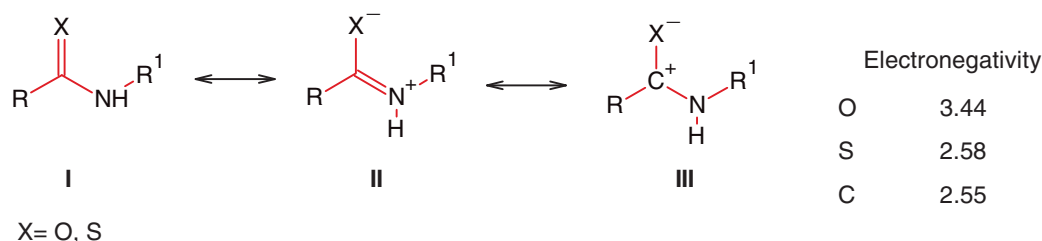
Scheme 1. Resonance structures of amides and thioamides.

and inexpensive tool to explore in detail their structural parameters and to know how the molecule interacts with each other or with a receptor.

Molecular electrostatic potential (ESP) [10] is extensively used to interpret and predict the reactive behaviour of a wide variety of chemical systems in electrophilic and nucleophilic reactions and hydrogen bonding interactions. The ESP is also suitable for analysing the identification process between a receptor drug and the enzyme-substrate interaction because species are recognised each other primarily through its potential. As previously proposed by Politzer *et al* [11], ESP can be a useful tool to predict and interpret nucleophilic processes. Another approach is given by Bader's Atoms in Molecules Theory [12], which reformulates chemical concepts like atoms, molecules, electron pairs or reactivity from the point of view of electronic density, $\rho(r)$. Like ESP, this is an observable physical magnitude independent from any arbitrary partition of the molecular orbital space. This concept is in agreement with the essence of the density functional theory, which establishes that total electronic density is a fundamental magnitude for any electronic system [13].

Lattice energies and intermolecular interaction energies associated to different molecular pairs are calculated to determine the energy components contributing to crystal stabilisation [14,15]. Hirshfeld surfaces analysis [16,17] is used for exploration of the packing modes and visualisation of intermolecular interactions. Quantitative pictures of intermolecular contacts, including the relative percentage of each type of interaction, are obtained from fingerprint plots and their decompositions [18,19]. Furthermore, the intermolecular interactions are analysed in terms of a combined quantitative study based on molecular dipole moments (μ) and ESP maps.

In this work, a new thiourea derivative, 1-butyl-3-(1-naphthoyl)thiourea (henceforth **1**), was synthesised and studied by theoretical and spectroscopic methods. This compound consists of a naphthyl ring and a butyl chain connected by successive amide C(=O)-NH and thioamide C(=S)-NH functions. The C=O and C=S bond length differ significantly and the π bond also might be expected to be strongly affected in the latter, due to the ineffective p-orbital overlapping between first and second

row atoms [20]. Due to the electronegativity difference between the of oxygen and carbon atoms [C =O ↔ C$^+$– O$^-$], the second charged resonance form of carbonyl is more important that in the case of thiocarbonyl [21]. For amides and thioamides, three major tautomeric forms can be drawn (Scheme 1), but the importance of **III** is drastically reduced in thioamides due to the small Pauling electronegativity difference between S (2.58) and C (2.55) atoms (the C=S bond has a small polarisation). In contrast, the larger sulphur size allows a greater charge transfer from N to S increasing the weight of form **II** in thioamides and also its rotational barrier around C-N bond [22]. Moreover, comparing amides and thioamides, the solvent effect on the rotational barrier is larger in the latter due its higher ground-state dipole moment and there is an important change in dipole moment with increasing solvent polarity [23].

2. Experimental

2.1. Instrumentation

2.1.1. Infrared and Raman spectroscopy
Infrared absorption spectra of **1** were measured on a Bruker EQUINOX 55 and LUMEX InfraLUM FT-02 spectrometers (resolution of 2 cm^{-1}) in the 4000–400 cm^{-1} range, using KBr pellets. Raman dispersion spectra of the solid, at room temperature, were recorded on a Thermoscientific DXR Raman microscope (spectral resolution 4 cm^{-1}) and the 532 nm radiation line of a diode-pump solid state laser was used for excitation in the 3500–100 cm^{-1} spectral range.

2.1.2. NMR spectroscopy
The ^{1}H and ^{13}C Nuclear Magnetic Resonance (NMR) spectra of **1** were recorded on a Bruker Avance 300 and Bruker Avance 250, respectively, using CDCl$_3$ as solvent and TMS as internal standard.

2.1.3. UV-Visible spectroscopy
Electronic spectra, using methanol as solvent, were carried out on a ChromTech CT-5700 UV/Vis spectrophotometer at 2.0 nm spectral bandwidth using

a quartz cell (10 mm optical path length). They were recorded in the spectral range of 190–1100 nm.

2.1.4. X-ray diffraction data

The measurements were performed on an Oxford Xcalibur, Eos, Gemini CCD diffractometer with graphite-monochromated MoKα ($\lambda = 1.54\,184$ Å) radiation. X-ray diffraction intensities were collected (ω scans with ϑ and κ-offsets), integrated and scaled with CrysAlisPro [24] suite of programs. The unit cell parameters were obtained by least-squares refinement (based on the angular settings for all collected reflections with intensities larger than seven times the standard deviation of measurement errors) using CrysAlisPro. Data were corrected empirically for absorption employing the multi-scan method implemented in CrysAlisPro.

The structure was solved by direct methods with SHELXS of the SHELX suit of programs [25]. The molecular model was refined by full-matrix least-squares procedure with SHELXL of the same package. The hydrogen atoms were positioned on stereo-chemical basis and refined with the riding model. The position of the H-atoms in the methyl group was optimised by treating this group as a rigid one which was allowed to rotate around the C-CH$_3$ bond during the refinement such as to maximise the sum of the residual electron density at the calculated H-positions. As a result, the methyl converged to a staggered rotational conformation. Crystal data, data collection procedure and refinement results are summarised in Table 1.

Crystallographic structural data have been deposited at the Cambridge Crystallographic Data Centre (CCDC). Enquiries for data can be direct to: Cambridge Crystallographic Data Centre, 12 Union Road, Cambridge, UK, CB2 1EZ or (e-mail) deposit@ccdc.cam.ac.uk or (fax) +44 (0) 1223 336 033. Any request to the Cambridge Crystallographic Data Centre for these materials should quote the full literature citation and the reference number CCDC 1557 949.

2.2. Synthesis of 1

Following a similar procedure to that described by Zaid *et al.* [26], a solution of 1-naphthoyl chloride (1.4 mmol) in dry acetonitrile (20 mL) was added dropwise to a suspension of potassium thiocyanate (2.8 mmol) in acetonitrile (10 mL) and the reaction mixture was refluxed with magnetic stirring for 1 h. The reaction flask was cooled at room temperature and then placed into a crushed ice bath. A solution of n-butylamine (1.7 mmol) in dry acetonitrile (10 mL) was added dropwise into the cooled

Table 1. Crystal data and structure refinement results for **1**.

Empirical formula	C$_{16}$H$_{18}$N$_2$OS
Formula weight	286.38
Temperature	293(2) K
Wavelength	1.54 184 Å
Crystal system	Triclinic
Space group	$P\bar{1}$
Unit cell dimensions	$a = 6.4045(6)$ Å
	$b = 10.8469(5)$ Å
	$c = 11.8669(9)$ Å
	$\alpha = 104.895(5)°$
	$\beta = 99.550(7)°$
	$\gamma = 92.139(5)°$
Volume	782.9(1) Å^3
Z, density (calculated)	2, 1.215 Mg/m^3
Absorption coefficient	1.806 mm^{-1}
F(000)	304
ϑ-range for data collection	3.920 to 70.986°.
Index ranges	$-7 \leq h \leq 7, -8 \leq k \leq 13, -14 \leq l \leq 14$
Reflections collected	5240
Independent reflections	2998 [R(int) = 0.0254]
Observed reflections [I>2σ(I)]	2420
Completeness to $\vartheta = 67.684°$	99.9%
Refinement method	Full-matrix least-squares on F^2
Data/restraints/parameters	2998/0/182
Goodness-of-fit on F^2	1.049
Final R indices [I>2σ(I)]	$R1 = 0.0566$, $wR2 = 0.1663$
R indices (all data)	$R1 = 0.0668$, $wR2 = 0.1844$
Extinction coefficient	n/a
Largest diff. peak and hole	0.517 and -0.301 e.Å^{-3}

^{a} $R_1 = \Sigma ||F_o|-|F_c||/\Sigma |F_o|$, $wR_2 = [\Sigma w(|F_o|^2-|F_c|^2)^2/\Sigma w(|F_o|^2)^2]^{1/2}$

mixture (-5 °C) and keep under stirring 1 h. The reaction was poured into cold water and the precipitated solid recrystallised in aqueous ethanol (Scheme 2) [14].

2.3. Quantum chemical calculations

Optimisations of the most stable conformers of **1** were performed applying the B3LYP method in combination with the standard split-valence basis sets 6-311++G(d,p). For the prediction of electronic transitions, the polarisable continuum model (C-PCM) [27–32] was used to include the solvent effect on the rotational isomerism.

To evaluate the relative stability of the molecule, isolated and in solution, Natural Bond Orbital (NBO) energy decomposition scheme (NBO 4.0 code [33]) was applied at the B3LYP/6-31G(d) level. Besides, a reactivity analysis of the **1** was carried out within Bader's Atoms In Molecules theory (AIM) [12] by using AIM2000 code [34]. All these methodologies were performed with the program package Gaussian 09 [35].

2.4. Lattice and interaction energies

To compare **1** with similar compound containing the N-(1-naphthoyl)thiourea moiety, five related crystal structures were obtained from Cambridge Structural Database
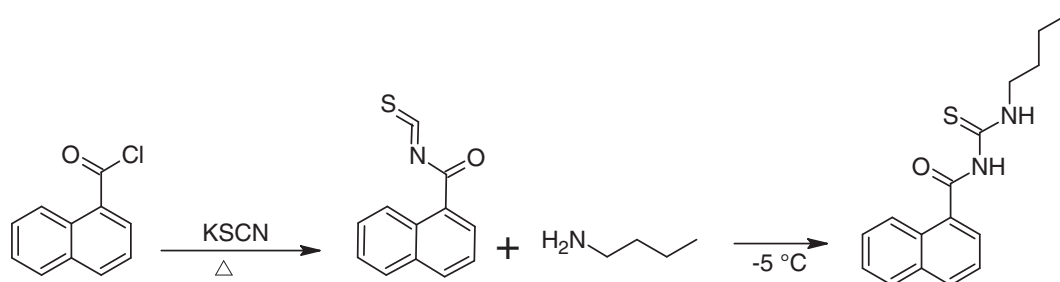
Scheme 2. Synthesis of **1**.

(CSD), with their refcodes being AJIQAN [36], MUL-MUD [37], MULNAK [37], XATSET [38], and XATRUI [38]. For each crystal under consideration, lattice energy and intermolecular interaction energies for specific molecular pairs were calculated with the MP2 method and 6-31G(d,p) basis set, using the CLP (Coulomb–London–Pauli) approach implemented in the PIXEL program package [39,40]. It enables partitioning of the total energy into their coulombic, polarisation, dispersion and repulsion contributions.

2.5. Hirshfeld surface calculations

Hirshfeld surfaces and their associated two-dimensional (2D) fingerprint plots [41–44] were plotted using CrystalExplorer3.0 software [45]. The d_{norm} (normalised contact distance) surface and the breakdown of 2D fingerprint plots were used for decoding and quantifying intermolecular interactions in the crystal lattice. The fingerprint plots can be decomposed to highlight particular atom pair close contacts [46], which overlap in the full fingerprint. The d_{norm} is a symmetric function of distances to the surface from nuclei inside and outside the Hirshfeld surface (di and de, respectively), relative to their respective van der Waals radii. The surfaces were mapped over a fixed colour scale of −0.050 au (red) – 0.130 Å au (blue). The 2D fingerprint plots were displayed by using the translated 0.6–2.6 Å range, including reciprocal contacts. ESPs on 0.008 eÅ^{-3} isosurfaces were calculated at the HF/6-31G* level by using Tonto program [47] integrated into CrystalExplorer.

2.6. Molecular electrostatic potentials

To find more evidences on the particular electrostatic nature of intermolecular N–H···S hydrogen bonds, molecular ESPs and dipole moments for compounds **1**, MULMUD, MULNAK, XATSET and XATRUI were computed from experimental electron distributions (for

method and basis set see Section 2.5), which are determined from X-ray diffraction data [42,48]. The experimental dipole moment of the molecules was calculated with the MP2 method and 6-31G(d,p) basis set.

3. Results and discussion

3.1. Crystal structure description

A drawing of the crystal packing is shown in Figure 1 and selected bond lengths and angles are listed in Table 2. As expected from extended π-bonding, the naphthyl group is planar (the maximum deviation from the best
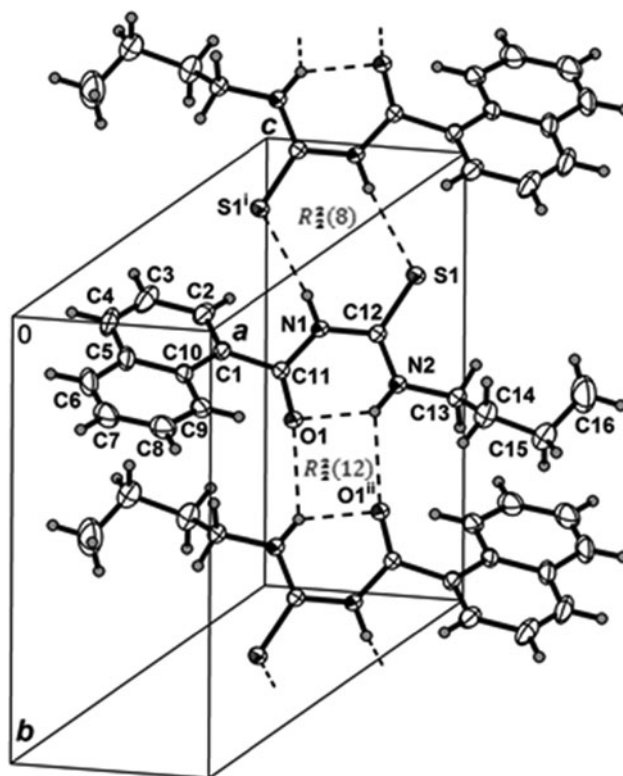

Figure 1. View of the crystal packing for **1**, showing the labelling of the non-H atoms. H-bonds are indicated by dashed lines. Space group symmetry operations: (1) -x+2, -y, -z+1; (2) -x+2, -y+1, -z+1.

Table 2. Selected bond lengths [Å] and angles [°] for **1**.

Param.	Exp.[a]	Calc.[b]	Param.	Exp.[a]	Calc.[b]
r(C1-C2)	1.371(4)	1.383	∠(C7-C6-C5)	122.3(3)	120.9
r(C1-C10)	1.428(3)	1.435	∠(C6-C7-C8)	119.9(3)	119.8
r(C1-C11)	1.497(3)	1.500	∠(C9-C8-C7)	121.0(4)	120.9
r(C2-C3)	1.414(4)	1.410	∠(C8-C9-C10)	121.0(3)	120.8
r(C3-C4)	1.348(6)	1.372	∠(C1-C10-C9)	123.9(2)	123.7
r(C4-C5)	1.404(6)	1.419	∠(C5-C10-C1)	117.6(3)	118.1
r(C5-C6)	1.438(6)	1.420	∠(C5-C10-C9)	118.5(3)	118.2
r(C5-C10)	1.425(3)	1.434	∠(N1-C11-C1)	114.40(17)	114.3
r(C6-C7)	1.338(7)	1.373	∠(O1-C11-C1)	122.40(19)	123.1
r(C7-C8)	1.389(6)	1.413	∠(O1-C11-N1)	123.16(18)	122.6
r(C8-C9)	1.363(4)	1.375	∠(N1-C12-S1)	118.10(14)	117.8
r(C9-C10)	1.414(4)	1.421	∠(N2-C12-N1)	117.07(18)	115.7
r(C11-N1)	1.371(3)	1.383	∠(N2-C12-S1)	124.83(16)	126.5
r(C11-O1)	1.220(3)	1.227	∠(N2-C13-C14)	111.6(2)	113.1
r(C12-N1)	1.392(3)	1.408	∠(C15-C14-C13)	115.0(3)	112.3
r(C12-N2)	1.318(3)	1.336	∠(C16-C15-C14)	112.8(4)	112.9
r(C12-S1)	1.675(2)	1.677	∠(C11-N1-C12)	128.15(17)	129.6
r(C13-C14)	1.507(5)	1.533	∠(C12-N2-C13)	124.77(19)	124.5
r(C13-N2)	1.461(3)	1.460	Φ(C1-C11-N1-C12)	− 174.8(2)	− 175.0
r(C14-C15)	1.512(5)	1.532	Φ(C2-C1-C11-N1)	49.6(3)	43.2
r(C15-C16)	1.437(7)	1.532	Φ(C2-C1-C11-O1)	− 128.4(3)	− 136.1
∠(C2-C1-C10)	121.4(2)	120.1	Φ(C10-C1-C11-N1)	− 134.9(2)	− 139.3
∠(C2-C1-C11)	118.7(2)	118.8	Φ(C10-C1-C11-O1)	47.1(3)	41.3
∠(C10-C1-C11)	119.7(2)	120.9	Φ(C14-C13-N2-C12)	99.1(3)	90.1
∠(C1-C2-C3)	119.(3)	121.3	Φ(N1-C12-N2-C13)	178.2(2)	179.9
∠(C4-C3-C2)	120.4(3)	119.8	Φ(N2-C12-N1-C11)	3.8(4)	− 0.1
∠(C3-C4-C5)	121.9(3)	121.0	Φ(N2-C13-C14-C15)	171.7(3)	179.6
∠(C4-C5-C6)	123.6(3)	120.9	Φ(O1-C11-N1-C12)	3.2(4)	4.4
∠(C4-C5-C10)	119.2(3)	119.7	Φ(S1-C12-N1-C11)	− 176.51(18)	179.4
∠(C10-C5-C6)	117.2(4)	119.4	Φ(S1-C12-N2-C13)	− 1.5(4)	0.6

[a] Experimental data from X-ray diffraction.
[b] Computed parameters for the most stable conformer **1a** (B3LYP/6-311++g(d,p)).

plane of the ten non-H atoms is 0.0498(1) Å for C8 atom), with C–C distances in the range from 1.338(7) to 1.437(6) Å, which corresponds to a resonant-bond structure. Carbonyl (C=O) and thiocarbonyl (C=S) double bond lengths are 1.220(3) Å and 1.675(2) Å, respectively. These values agree with the difference found between carbonyl and thiocarbonyl groups, as expected, a C=S bond length (∼1.6 Å) considerably longer than C=O (∼1.25 Å) [20]. It is interesting to note that the shortest C–N bond length belongs to C12-N2 (1.318 Å) followed by C11-N1 (1.371 Å) (see Table 2). The significant differences between them suggest a strong π-donation from N2 resulting in an increase in electron density at both carbon and sulphur atoms of the thioamide function (form **II** in Scheme 1)[23].

An intramolecular NH···O hydrogen bond [d(N···O) = 2.672(2) Å, ∠(N–H···O) = 135.4°] favours the observed nearly planar carbonylthiourea C(O)NHC(S)NH group (the maximum deviation from the best plane of the six non-H atoms is 0.0703 (1) Å for O1 atom), which subtends a dihedral angle of 53.81(8)° with the naphthyl plane. Besides, the detected weak intramolecular interaction between C9-H9···O [d(H9···O) = 2.527 Å, ∠(C9-H9···O) = 115.0°] contributes to the adopted conformation in the solid.

Table 3. Intra and intermolecular hydrogen bond distances and angles in **1**.

D-H···A	d(D-H)	d(H···A)	d(D···A)	∠(DHA)
N(1)-H(1) ··S(1)#1	0.86	2.58	3.391(2)	158.2
N(2)-H(2A) ··O(1)	0.86	1.99	2.672(2)	135.4
N(2)-H(2A) ··O(1)#2	0.86	2.45	3.113(2)	134.8

Symmetry transformations used to generate equivalent atoms:
(#1) -x+2, -y, -z+1; (#2) -x+2, -y+1, -z+1.

As shown in the crystal packing of Figure 1, neighbouring molecules are arranged in centrosymmetric dimers with $R_2^2(12)$ motifs linked through intermolecular N–H···O hydrogen bonds [d(N···O) = 3.113(2) Å, ∠(N–H···O) = 134.8°]. The dimers, in turn, are connected to each other by intermolecular N–H···S bonds [d(N···S) = 3.391(2) Å, ∠(N–H···S) = 158.2°] giving rise to polymeric ribbons ($R_2^2(8)$) extended along the crystal b-axis (see Table 3). For more parameters, see Tables S1-S3, ESI†).

3.2. Conformational analysis

The conformational study of **1** allowed to predict two conformers, **1a** and **1b,** as the most stable, being **1b**
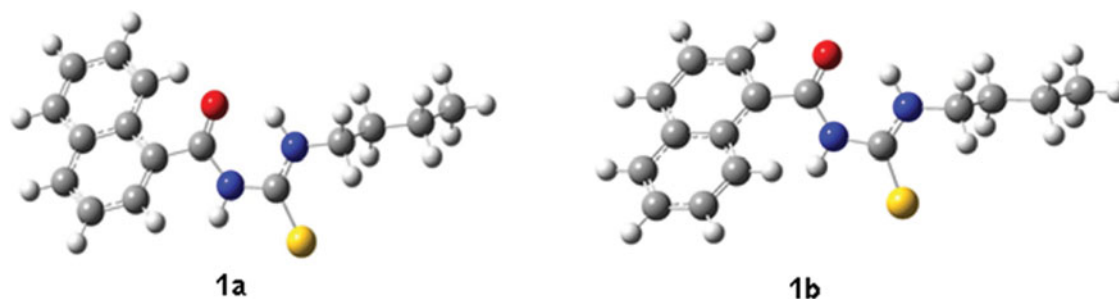
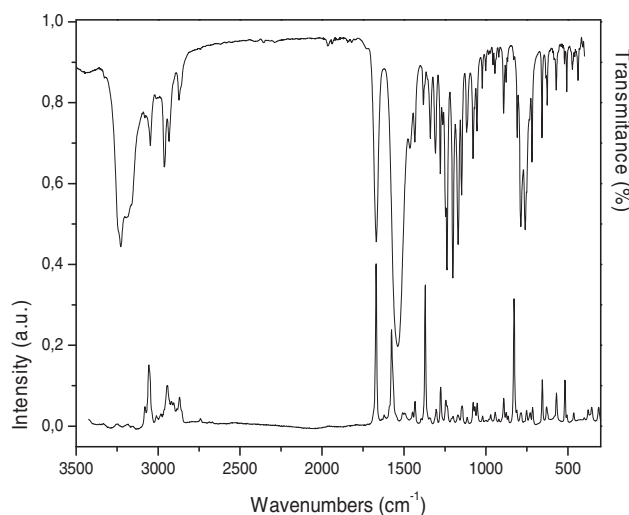**Figure 2.** Optimised structures of conformers **1a** and **1b**.

Figure 3. Infrared spectrum of the solid (upper trace, KBr pellets) and Raman spectrum (lower trace) of **1.**

Table 4. Experimental, calculated and tentative assignment of relevant vibrational modes for **1a** and **1b.**

Experimental[a]		B3LYP/6-311++g(d,p)[c]		
IR[b]	Raman[b]	**1a**	**1b**	Assignment[d]
3327 vw	3352 vw	3612 (36)	3607(38)	ν(N1-H1)
3227 m	3184vw	3452 (277)	3440(260)	ν(N2-H2A)
1669 m	1671 s	1709(194)	1714(263)	ν(C=O)
1537 s	1576 s	1594(348)	1597(401)	ν(C-N)$_{But}$
1118 vw	1115 vw	1125 (24)	1126(39)	ν(C-N)$_{C=O}$
734 vw	732 vw	744(11)	746(13)	ν(C-S)

[a] in cm^{-1}.
[b] s, strong; m, medium; w, weak; vw, very weak; Sh: Shoulder.
[c] Calculated IR frequencies (cm^{-1}) and intensities (km mol^{-1}) in parentheses.
[d] ν and δ represent stretching and in plane deformation, respectively.

$\sim$0.6 kcal/mol higher in energy (Figure 2). The populations according to Boltzmann equation are 72% and 28% for **1a** and **1b**, respectively (see Figures S4 and S5, ESI†). The structural difference between the predicted conformations is related to the orientation of the naphthyl ring relative to the carbonyl thiourea core. The naphthyl ring in **1b** has the H-2 atom towards the carbonyl group (ΦC10C1C11O1 = $-$139.7°) giving rise a pseudo five-membered ring. However, in **1a** the H-9 of the naphthyl ring is oriented towards the C=O group (the calculated torsion angle C10C1C11O1 is 41.3°), originating a most stable pseudo six-membered ring favouring this preferred conformation (see Figure 2) which is coincident with the X-ray elucidated structure. The experimental and calculated (**1a**) bond lengths and angles shown in Table 2 reveal a very good agreement.

3.3. Vibrational spectroscopy

A complete tentative assignment of the experimental IR and Raman spectra (Figure 3) was performed, by inspection of the corresponding calculated spectra for the most stable conformer **1a** and reported values for related compounds (see Table S6 ESI†). Some relevant vibrational modes and the corresponding computed values for both conformers are shown in Table 4.

The N–H stretching is observed as very weak and medium bands at 3327 and 3227 cm^{-1}, respectively. The former was attributed to the N–H bonded to the carbonyl carbon atom, considering the well-known electron withdrawing effect of the carbonyl oxygen atom. The N2-H2A donor forms intramolecular hydrogen bond interactions with the acceptor oxygen atom, so that the band is shifted to lower wavenumbers with increased intensity (calc. 3612 and 3452 cm^{-1} for **1a** and 3607 and 3440 cm^{-1} for **1b**). The C=O stretching appeared in IR as a strong band at 1669 cm^{-1} and at 1670 cm^{-1} in Raman, being the latter the most intense band of the spectrum (calc. 1709 (**1a**) and 1714(**1b**)). The absorptions localised at 1537 and 1118 cm^{-1} in IR and at 1575 and 1115 cm^{-1} in Raman are assigned to the C-N stretching attached to the butyl and carbonyl moieties, respectively. The difference between the observed frequencies of both C-N bonds is attributed to the partial double character of the N-C bond with the butyl substituent on the nitrogen atom.
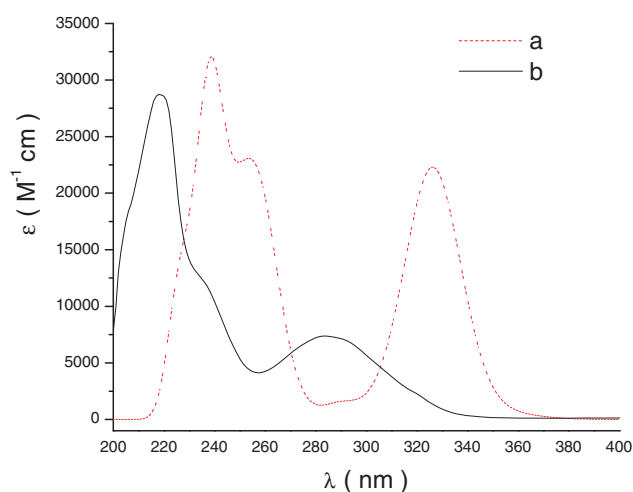
Figure 4. Calculated (**a**) and experimental (**b**) electronic spectra (B3LYP/6-311++G(d,p) of **1**.

The C-S stretching is assigned to the bands at 734 (IR) and 731 (Raman) cm^{-1}. The location of this band suggests the single character of this bond (calc. 744 (**1a**) and 746 (**1b**) cm^{-1}).

3.4. Electronic spectra

The experimental and calculated electronic absorption spectra of **1** are shown in Figure 4. The wavelengths of the main observed bands, the corresponding calculated values and a tentative assignment of the electronic transitions are presented in Table 5. Only the dominant transitions ($f > 0.06$) were taken into account to assign the observed bands (the main molecular orbitals involved in the electronic transitions are depicted in Figure S7 ESI†).

The shoulder observed at 204 nm is due to the contribution of one electron transition HOMO→LUMO+4 (calc. 226 nm) which is originated by excitations from non-bonding orbitals of the sulphur atom to the π^* orbitals of the aromatic rings and carbonyl group. The

Table 5. Experimental and calculated electronic spectrum of **1** in acetonitrile solution, along with relevant transitions assignments.

Experimental[a]	calculated[b]	f[c]	Assignment	%
204^{sh}	226	0.0612	HOMO → LUMO+4	68
218	238	0.2927	HOMO-5 → LUMO	87
236	251	0.1295	HOMO-3 → LUMO	20
			HOMO-3 → LUMO+1	34
			HOMO-1 → LUMO+2	36
	259	0.1434	HOMO-2 → LUMO+1	100
284	327	0.212	HOMO-1 → LUMO	92

^{a} in nm.
^{b} Calculated electronic transitions (B3LYP/6-311++G(d,p) for the most stable conformer **1a**.
^{c} The oscillator strength of the transitions calculated in atomic units. sh: Shoulder.

band at 218 nm corresponds to excitations from HOMO-5 to LUMO orbitals. The absorption is generated by transitions from to the π^* of the fused aromatic rings to the non-bonding orbitals of the sulphur atom. The shoulder localised at 236 nm (calc. 251 and 259 nm) is attributed principally to one-electron excitations HOMO-3 → LUMO, HOMO-3 → LUMO+1, HOMO-1 → LUMO+2 and HOMO-2 → LUMO+1. The shoulder comes basically from contributions of π orbitals of the naphthyl moiety, non-bonding orbitals of oxygen, nitrogen and sulphur atoms to π^* orbitals of the aromatic rings. The band centred at 284 nm is dominated by transitions from HOMO-1 to LUMO (92%) corresponding to $\pi \rightarrow \pi^*$ excitations within the aromatic skeleton.

The shape of the electronic spectrum agrees acceptably with the experimental one, although the calculated maxima are shifted to lower wavelengths (see Figure 4). The efforts of theoretical chemistry to approximate calculated electronic spectra closer to experimental ones have been considered in a recent publication by a performance comparison of electronic excitation calculation methods for a set of compounds [49].

3.5. NMR spectroscopy

The NMR chemical shifts of N–H protons showed broad singlets at 10.74 and 8.99 ppm. The most deshielding value was assigned to the BuN–H proton, connected to the carbonyl oxygen atom via intramolecular hydrogen bond (BuN–H···O). The ^{1}H NMR of the naphthoyl moiety were compared with reported values for naphthoyl esters [50]. The most deshielded aromatic proton corresponds to H9 and agree with the calculated most stable conformation **1a** (see Section 3.2.), that predict a hydrogen bond interaction for this nucleus. The atom numbering was taken from Figure 1. The C–H carbon atoms were distinguished from the quaternary carbon signals through the DEPT spectrum (by comparison with the ^{13}C NMR one). The COSY spectrum allowed the unambiguous assignment of aromatic protons (see Figures S10 and S11, ESI†).

^{1}H NMR (300 MHz, CDCl$_3$) $\delta = 10.74$ (br.s, 1H, Bu-NH); 8.99 (s, 1H, O=C-NH); 8.31 (dd, 1H, H9, $J = 8$ and 1 Hz); 8.02 (d, 1H, H2, $J = 8$ Hz); 7.91 (dd, 1H, H4, $J = 7$ and 2 Hz); 7.74 (dd, 1H, H6, $J = 7$ and 1 Hz); 7.60 (dt, 2H, H8 and H7, $J = 7$ and 8 Hz); 7.50 (dd, 1H, H3, $J = 8$ and 7 Hz); 3.74 (dt, 2H, N-CH$_2$, $J = 7$ and 5 Hz); 1.75 (q, 2H, NCH$_2$C$\underline{H}_2$, $J = 7$ Hz); 1.49 (sext, 2H, CH$_3$C$\underline{H}_2$, $J = 7$ Hz); 1.01 ppm (t, 3H, CH$_3$, $J = 7$ Hz).

^{13}C NMR (75 MHz, CDCl$_3$) $\delta = 179.9$ (C=S); 169.1 (C=O); 133.9 (C1); 133.0 (C2); 131.0 (C10); 129.9 (C4); 128.9 (C5); 128.3 (C6); 127.1 (C7); 126.3 (C3); 124.7

Table 6. Important hyperconjugative interactions of the natural bond orbitals for **1**, calculated using B3LYP/6-311++G(d,p).[a]

	Isolated		Acetonitrile solution	
	kcal mol^{-1}			
	1a	1b	1a	1b
LP(1)O1 → σ*C1-C11	1.30	1.22	1.30	1.30
LP(1)O1 → σ*C11-N1	2.18	2.21	2.19	2.19
LP(1)O1 → σ*N2-H2A	2.58	2.81	2.57	2.54
LP(2)O1 → π*C1-C11	17.69	18.05	17.67	17.79
LP(2)O1 → π*C11-N1	23.38	23.33	23.28	23.24
LP(2)O1 → π*N2-H2A	7.81	8.46	7.83	7.88
LP(1)N1 → LP*C12	99.51	99.27	101.24	100.84
LP(1)N1 → σ*C11-O1	1.17	0.71	1.16	0.68
LP(2)N1 → π*C11-O1	50.29	53.91	49.68	53.22
LP(1)N2 → LP*C12	182.51	184.33	185.60	186.26
LP(1)N2 → σ*C13-H13A	1.60	1.69	1.73	1.74
LP(2)N2 → σ*C13-H13B	1.63	1.53	1.40	1.40
LP(1)N2 → σ*C13-C14	6.02	6.01	5.82	5.82
LP(1)N2 → σ*C14-C15	0.75	0.75	0.77	0.77
LP(1)S1 → σ*N1-C12	2.39	2.39	2.25	2.24
LP(1)S1 → σ*C12-N2	3.68	3.68	3.43	3.46
LP(2)S1 → σ*N1-C12	12.18	12.06	11.42	11.44
LP(2)S1 → σ*C12-N2	11.69	11.59	11.00	11.03
LP(1)S1 → LP*C12	369.68	365.24	346.00	348.71
Total	798.04	799.24	776.34	782.55

(C9); 124.6 (C8); 45.8 (N-CH$_2$); 30.4 (NCH$_2$$\underline{C}H_2$); 20.3 (CH$_3$$\underline{C}H_2$); 13.9 ppm (CH$_3$).

3.6. NBO analysis

The role of hyperconjugative interactions in the conformers stabilisation has been assessed using NBO analysis, where the hyperconjugation represents the transfer of an electron between a lone pair (LP) or bonding orbital and an antibonding orbital. As afore mentioned, the rotational barrier around the C–N bond is solvent dependent. The effect is greater on thioamides since for them the polarity changes between the basal and the rotational transition state is more pronounced [23]. For this reason, the calculations include also the evaluation in acetonitrile as solvent. It was chosen as a polar aprotic solvent (3.92 D) in order to detect the major differences and avoiding the rupture of intramolecular hydrogen bond interactions.

Table 6 contains the main hyperconjugative interactions for conformers **1a** and **1b**. In terms of NBO analysis, it was found that the hyperconjugation effect has a pendular behaviour with solvation for both conformers, but is more defined around the atoms belonging to amide and thioamide groups. Thus, LPs of the oxygen, nitrogen and sulphur atoms transfer electronic charge to the σ* orbital of C–C, C=O and C–N bonds. Furthermore, LPs of the oxygen atom in both forms transfer electronic charge to the virtually empty σ* orbital of the N2-H2A bond. The magnitude of the interaction is 7.81 and 8.46 kcal/mol (**1a** and **1b**, respectively) for the LP(2)O1→σ*N2-H2A, showing a remarkable decrease

for **1b** with the solvation. The most important hyperconjugative interactions were observed from the LP of nitrogen (1 and 2) and sulphur atoms to the antibonding orbital of the C12 atom (LP*C12) with values for **1a** of 99.51, 182.51 and 369.68 kcal mol^{-1} for LP(1)N1, LP(1)N2 and LP(1)S1, respectively. According to Table S14, it can be observed that C11 and C12 atoms bounded to the electronegative oxygen and sulphur atoms, respectively, have a positive charge. Although a high negative charge on sulphur would be expected, due to the ineffective π overlapping with C12 and the strong π-donation from N2, the high hyperconjugative stabilisation energy of 369.68 kcal mol^{-1} found for LP(1)S1 → C12 LP* is another way of justifying the C–S bond distance and its atomic charge. The more significative solvation effects were found around the sulphur atom (see the last five hyperconjugative interactions described in Table 6). These interaction energies decrease 5.8%–6.8% after solvation, whereas those around oxygen atom are scarcely affected. These results agree with the insight that the more polar thioamide group is better stabilised in solution than the amide function. Now, the solvent-stabilised sulphur LP are less available to hyperconjugative interaction.

3.7. AIM analysis

The quantum theory of Atoms in Molecules (AIM) has repeatedly shown to be helpful in bonds characterisation through a topological analysis of the electronic charge density and its Laplacian at the bond critical point (BCP) [12]. In this theory, the nature of a bonding interaction can be determined through an analysis of the properties of the charge density ρ and its Laplacian $\nabla^2 \rho$ at the BCP (the latter provides an enhanced view of the local form of the electronic density), the ellipticity (ε), the relationships between the perpendicular and parallel curvature ($|\lambda 1|/\lambda 3$) and the potential and kinetic energy densities ($|Vb|/Gb$) [12]. In Figure 5 are displayed the molecular graphs, formed by a network of bond paths (BPs), for conformer **1a.**

In Figure 5(a), big circles correspond to attractors or (3, −3) nuclear critical points (NBP, attributed to the positions of the atomic nuclei), lines connecting the nuclei are the BPs and the small circles are the BCP or (3, −1) critical points, obtained from topological analysis of the electronic density. The presence of a BP and its associated virial path provides an universal indicator of bonding between atoms.

Table 7 presents the BCPs for **1a**. As observed, the charge density at the C–S BCP is relatively high and its Laplacian $\nabla^2 \rho$ negative, indicating that the charge density is concentrated in the internuclear region. Besides,
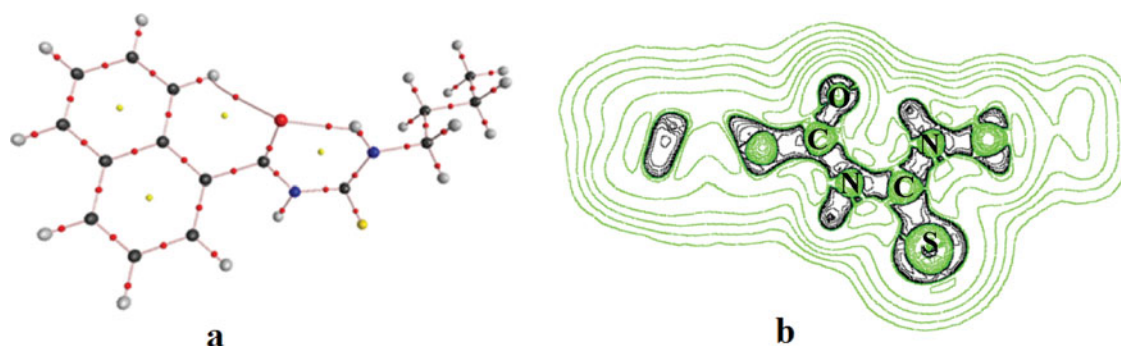
Figure 5. (a) Topological graphs for **1a** showing bond and ring paths (solid lines that join adjacent atoms and also those involved in hydrogen bonding interactions), and bond and ring critical points (small circles located along the bond paths and circles inside the rings and pseudo rings, respectively). **(b)** Contour map of the Laplacian, showing the same orientation of a) and atoms in the same plane (-CO-NH-CS-NH-) are indicated by circles.

whereas the $\rho(r_c)$ value for C–S bond decreases with solvation (isolated: 0.213; acetonitrile solution: 0.209), its bond length ($r(_c)$) increases (1.677 and 1.694 Å). Moreover, the charge of the C-S group turns after solvation from negative (−0.014, isolated) to slightly positive (+0.054, acetonitrile solution) (see Table S14). This behaviour indicates a bond polarisation when the molecule is solvated in a polar environment and agrees with the decreasing hyperconjugative effect observed in the NBO analysis of Section 3.6. This feature increases the reactivity of the C-S group in acetonitrile solution.

The contour map of $\nabla^2\rho$ for **1a** is shown in Figure 5(b). Solid lines enclosed by thick ones correspond to negative values of $\nabla^2\rho$, indicating areas of electron density concentration, whereas the lines around the atoms location and the most external to them are low electron density zones with positive values of $\nabla^2\rho$.

The values of $\rho(r)$ and $\nabla^2\rho(r)$ for the C–C ring, C–C chain and C–N bonds in the structures (isolated and in acetonitrile solution) are typical of a shared or covalent interaction (also $Vr/Gr > 1$ and $|\lambda 1|/\lambda 3 > 1$), which is dominated by a contraction of ρ towards the BP leading to its accumulation in the internuclear region.[51] When the molecule is solvated, a decrease in the covalent character of the C–C$_{ring}$ bond, (0.314 au (isolated) to 0.295 (solution)) is observed. For the C=O bond, the values of $\rho(r)$ and $\nabla^2\rho(r)$ are (isolated/solution): 0.399/0.398 au and −0.306/ −0.304 au, respectively [52,53].

For **1a**, the calculated $\nabla^2\rho(r)$ values that are large and negative indicate strong shared interactions, as in the case of C12-N2 (−0.992 au) and C12-N1 (−0.832 au).

Intramolecular N2-H2A···O1 and C9-H9···O1 hydrogen bonds are detected for **1a**. Charge density (0.032/0.014 au) and Laplacian (0.116/0.052 au) for both

Table 7. Local topological properties of the electron charge density calculated at B3LYP/6-311++G(d,p) for conformer **1a**.

BCP (3,−1)	Isolated						Acetonitrile solution					
	$r(_c)$	$\rho(r_c)$	$\nabla^2\rho(r_c)$	$|\lambda_1|/\lambda_3$	$\varepsilon = |\lambda_1|/\lambda_2 - 1$	$|V(r_c)|/G(r_c)$	$r(_c)$	$\rho(r_c)$	$\nabla^2\rho(r_c)$	$|\lambda_1|/\lambda_3$	$\varepsilon = |\lambda_1|/\lambda_2 - 1$	$|V(r_c)|/G(r_c)$
C–C[a]	1.421	0.314	−0.872	2.079	0.243	4.000	1.435	0.295	−0.800	1.813	0.151	4.260
C–C[b]	1.498	0.241	−0.548	1.283	0.043	4.466	1.389	0.240	−0.537	1.265	0.015	4.419
C1–C11	1.499	0.262	−0.652	1.445	0.094	4.640	1.496	0.263	−0.658	1.461	0.092	4.630
C11=O	1.226	0.399	−0.306	0.613	0.077	2.130	1.228	0.398	−0.304	0.612	0.072	4.634
C11–N1	1.383	0.305	−0.870	1.783	0.113	3.185	1.384	0.304	−0.871	1.784	0.105	3.187
N1–C12	1.408	0.290	−0.832	1.842	0.079	3.365	1.401	0.295	−0.861	1.885	0.085	3.383
N1–H1	1.010	0.341	−1.742	1.543	0.049	10.70	1.011	0.34	−1.760	1.570	0.047	11.17
C12–S	1.677	0.213	−0.111	0.722	0.072	2.110	1.694	0.209	−0.210	1.096	0.081	2.273
C12–N2	1.336	0.338	−0.992	1.855	0.192	3.072	1.329	0.343	−1.001	1.809	0.200	3.037
N2–C13	1.460	0.253	−0.626	1.642	0.025	3.089	1.463	0.250	−0.605	1.602	0.016	3.020
N2–H2A	1.018	0.332	−1.722	1.575	0.045	10.51	1.019	0.332	−1.741	1.591	0.042	10.82
C=O···H2A[c]	1.880	0.032	0.116	0.217	0.014	0.946	1.880	0.032	0.117	0.217	0.010	0.950
C=O···H9[c]	2.322	0.014	0.052	0.164	0.106	0.830	2.385	0.013	0.047	0.156	0.136	0.830
RCP (3, +1)												
C-C-C (a)		0.021	0.152	0.186	0.080	0.762		0.0210	0.152	0.187	−0.800	0.758
C-C-C (b)		0.0209	0.153	0.188	0.800	0.763		0.0207	0.152	0.188	−0.801	0.760
C=O···H2A-N2		0.012	0.060	0.126	0.605	0.758		0.059	0.102	0.189	−0.749	0.762
C=O···H9-C9[c]		0.0158	0.101	0.185	0.750	0.628		0.0108	0.057	1.117	−0.562	0.749

interactions are within the range proposed by Koch and Popelier [54]. In addition, the values of $|\lambda1|/\lambda3$ and $|Vb|/Gb$ are < 1 indicating intramolecular interactions. The last indicator reveals that the kinetic energy contribution is greater than the potential energy at the BCP. In contrast, at the BCP of a proton donor bond, the relationship $|\lambda1|/\lambda3$ is > 1 and $|Vb|/Gb$ is >> 1, as it occurs for N1-H1 (1.543/10.70) and N2-H2 (1.575/10.51).

The ρ values at C=O···H2A and C=O···H9 (0.032 and 0.014 au, respectively) and the Laplacian at the BCPs > 0 (0.116 and 0.052 au, respectively) are low, but higher for C=O···H2A by the more acidic character of H2A. This agrees with the shortest distance between O···H2A. Therefore, the BCPs are localised in an electron charge density depletion zone, indicating that the intramolecular interactions exhibit the features of closed shell interactions (typical values for H-bond are ρ: 0.002–0.040 au and $\nabla^2\rho$: 0.02–0.150 au) [55]. Furthermore, electron charge density and its Laplacian evidence the strength of the hydrogen bond [56]. As observed in Table 7, for the solvated molecule, the C=O···H2A interaction is not modified by the presence of the solvent, while the C=O···H9 hydrogen bond is slightly weakened. It should be noted that the last weak hydrogen bond is also detected in the solid state and is probably responsible for the conformation adopted **1a** (this interaction is not observed in **1b**). The AIM results are here important since they evidence the existence and strength of such weak intramolecular hydrogen bonding.

In contrast, at the BCP of a proton donor bond, the relationship $|\lambda1|/\lambda3$ is > 1 and $|Vb|/Gb$ is >> 1, as it occurs for N1-H1 (1.543/10.70) and N2-H2 (1.575/10.51). The values for the solvated molecule are slightly higher, showing stronger shared interactions in solution (see Table 7).

The C=O···H–N interaction plays an important role in stabilisation and reactivity of other molecule sites. In addition, the efficiency of oxygen as an electrophilic attack site decreases with the formation of a six-membered ring (through the intramolecular hydrogen bond), and the charge delocalisation towards other groups is favoured.

Table S15 (ESI†) shows topological properties of conformers **1a** and **1b** and Figure S13 (ESI†) the topological graph for **1b**. As observed, there are no significant differences between both conformations.

3.8. Structural motifs, lattice and intermolecular energies

A packing diagram of compound **1** is depicted in Figure 1. Each molecule forms dimeric $R_2^2(12)$ and $R_2^2(8)$ centrosymmetric ring motifs with neighbouring molecules, the former through strong N–H···O hydrogen bonds

Table 8. Lattice energies (kJ mol$^{-[1]}$) partitioned into coulombic (E_{coul}), polarisation (E_{pol}), dispersion (E_{disp}) and repulsion (E_{rep}) components for **1** and related compounds.

Compound	E_{coul}	E_{pol}	E_{disp}	E_{rep}	E_{TOT}
1	−79.1	−40.3	−165.8	126.6	−158.6
AJIQAN	−72.5	−40.2	−214.9	154.6	−172.9
MULMUD	−89.3	−43.7	−203.0	161.2	−174.7
MULNAK	−90.1	−45.3	−193.8	154.5	−174.6
XATSET	−82.4	−46.8	−191.2	156.2	−164.3
XATRUI	−77.8	−42.9	−174.1	135.0	−159.8

$[d(N···O) = 3.113(2)$ A, $\angle(N–H···O) = 134.8°]$ (Table 8, column 4) on the one side of thioureide moiety, and the latest *via* weak N–H···S hydrogen bonds $[d(N···S) = 3.391(2)$ A, $(N–H···S) = 158.2°]$ on the opposite side giving rise to ribbons extended along the *b*-axis.

Thioureas can basically form two different supramolecular motifs in the solid state such as 1D hydrogen-bonded chains (or cyclic chains) and dimers [57], the latest further associated into 2D hydrogen-bonded layers, ribbons or tapes [58] via two complementary N–H···S hydrogen bonds $[R_2^2(8)$ graph set]. The chain/dimer duality has been observed in *trans–cis* conformation for crystalline di-substituted alkylthioureas [59], and in a series of aromatic bis(thiourea) derivatives [60]. The dimer motif is only slightly more preferred than that of the chain [59], observed also in structures of aroylthioureas. The supramolecular architecture with two kinds of intermolecular N–H···S hydrogen bonds forming consecutive dimers that expand in ribbons has been found only for the crystal structure of unsubstituted N-benzoylthiourea [61]. Additionally, intermolecular N–H···O hydrogen bonds are not common in mono-substituted aroylthioureas. A pattern of weak bifurcate N–H···O and N–H···S intermolecular hydrogen bonds, joining molecules into a rare one-dimensional (1D) ladder-like structural motif, was recently found in a dithiourea derivative [62]. These facts confirm that the hydrogen bonding network in **1** represent a novel packing mode for this type of compounds, which may be useful as building block in crystal structure design [57].

In order to compare the packing mode of **1** with similar structures, energetic calculations were performed for three N'-substituted (1-naphthoyl)thioureas with the following refcodes: AJIQAN [36], MULMUD [37] and MULNAK [37], and two N'-dialkyl-N-(1-naphthoyl)thioureas (refcodes XATSET [38], and XATRUI [38]).

Lattice energy calculations (Table 8) show that the dispersion energy (E_{disp}) is the major contribution towards the crystal stabilisation for all compounds as generally expected for organic species, with similar percentages ranging from 58.1% in compound 1%–65.6% in AJIQAN. However, the coulombic component (E_{coul}) is similar

and significant for all structures representing the second higher contributor ranging from 22.1% (AJIQAN) to 31.8% (compound **1**). We observed that the lattice energies are highest and very similar for pyridinethiourea (AJIQAN) and the two phenylthioureas (MULMUD and MULNAK), indicating the relevant role of aromatic substituents in the crystal stabilisation of these compounds, when compared to alkyl substituents (**1**, XATSET and XATRUI). Curiously, significant changes are not observed in the total lattice energies of the two *N*'-dialkyl-substituted- compared to *N*'-monoalkyl-substituted-naphthoylthiourea (compound **1**).

Intermolecular energy calculations from selected molecular pairs are shown in Table 9. The occurrence of N–H···S hydrogen bonds forming dimers with $R_2^2(8)$ motifs is a common feature for all structures except in AJIQAN, generating molecular pairs with highest energy stabilisation (from −66.6 kJ/mol for XATRUI to −70.5 kJ/mol for MULNAK) in comparison with molecular pairs involving other types of contacts. In structure AJIQAN is distinctive patterns of weak intermolecular C–H···S and C–H···O hydrogen bonds, as well as π···π contacts similar to analogous benzoylthiourea compounds [63], being the last contacts involved in a molecular pair with −49.6 kJ/mol (calculated for us) as maxima intermolecular energy. However, the naphthoylthiourea derivative (AJIQAN) differs in the appearance of intermolecular N–H·· ·C hydrogen bonds in a molecular pair where interaction energy increases to −63.3 kJ/mol. It is interesting to notice in structures **1**, MULMUD and MULNAK that the total energy in molecular pairs involving N–H···S hydrogen bonds is significantly higher than that involving classic N–H···O hydrogen bonds with lower inter-centroid and H···O (**1** and MULMUD) distances. This can be explained considering that the more electronegative (and basic) oxygen atom also participates as an acceptor in the intramolecular N–H···O hydrogen bonds as shown in Figure 1 and therefore the total negative charge is distributed around the periphery of the O1 atom. PIXEL intermolecular energies also reveal that the highest contribution towards the crystal stabilisation comes from coulombic component (40.8%–44.3%) only for molecular pairs involving N–H···S interactions, while the dispersion energy is clearly dominant for remaining interactions.

3.9. Hirshfeld surface analysis

For a better comprehension of the crystal packing for studied compounds, a complete description of the main intermolecular interactions using Hirshfeld surface analysis have been carried out. Figure 6(a,b) shows surfaces mapped over the d_{norm} property for compound **1**, while
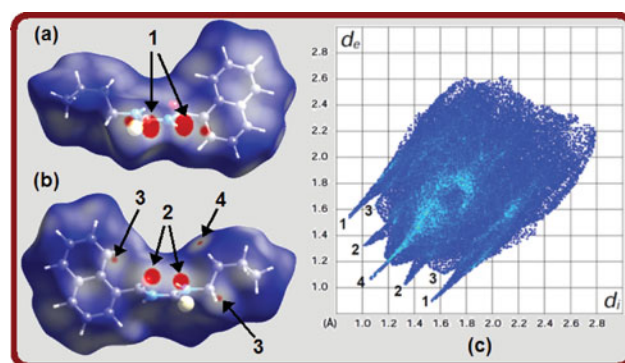

Figure 6. Views of the Hirshfeld surfaces of **1** mapped with d_{norm} in two orientations: (a) front view, (b) back view (180° rotated around the vertical axis of the plot). Full two-dimensional fingerprint plot is shown in (c). Close contacts are labeled as follows: (1) S···H, (2) O···H, (3) C···H and (4) H···H.

the Hirshfeld surfaces for the five related structures can be seen in Figure S16 (ESI†). Key contacts are indicated by arrows with numbers. The surfaces are shown as transparent to allow visualisation of the molecules. Contacts with distances equal to the sum of the van der Waals radii are represented as clear regions and the contacts with distances shorter than and longer than van der Waals radii are shown as dark circles and intermediate intensity colour areas, respectively.

Two largest and dark regions labelled 1 in Figure 6(a,b) are dominant in the d_{norm} map, and represent H···S/S···H contacts attributed to N1–H1···S1 hydrogen bonds in agreement with packing diagram (Figure 1) and highest interaction energy of −67.6 kJ/mol. A pair of large and dark spots labelled 2 shows H···O/O···H contacts associated to N2–H2A···O1 hydrogen bonds, whereas two small regions labelled 3 on the surface (Figure 6(a)) correspond to H···C/C···H contacts associated to weak C13-H13B·· ·C9 hydrogen bonds. Both types of contacts are involved in the same molecular pair with interaction energy of −60.5 kJ/mol. It is worthwhile to indicate that H···H contacts (labelled 4) represent the weakest interaction (−22.2 kJ/mol) in compound **1**. Although the H···H contacts are also present in the remaining structures, are not visible due to the contact distances are longer than the sum of the van der Waals radii.

Full 2D-fingerprint plot of the main intermolecular contacts for title compound and related structures are depicted in Figure 6c and Figure S16 (ESI†), respectively. The relative contributions of individual intermolecular interactions to the Hirshfeld surface area for all six structures are shown in Figure 7. A similar contribution of S···H (9%–14%) and O···H (5%–7%) contacts in all structures were observed. These interactions are identified by a sharp spike at the bottom right region ($d_e < d_i$) of the

Table 9. Interaction energies (E_{TOT}) partitioned into coulombic, polarisation, dispersion and repulsion contributions (kJ mol^{-1}[1]) for various molecular pairs in **1** and related compounds.

Compound	Symmetry	Involved interactions	d(H···A), $\angle D$—H···A	Centroid distance	E_{coul}	E_{pol}	E_{disp}	E_{rep}	E_{TOT}
1	2-x,-y,1-z	N1-H1···S1	2.577(1), 158	6.192	− 64.3	− 44.0	− 44.4	85.1	− 67.6
	2-x,1-y,1-z	N2-H2A···O1,	2.447(2), 135	5.383	− 32.1	− 10.9	− 57.4	40.0	− 60.5
	3-x,1-y,1-z	H14B···H14B	2.3553(2)^a	8.727	− 6.7	− 4.0	− 29.9	18.3	− 22.2
AJIQAN	1-x,1-y,1-z	N1-H1···C5,*	2.63(2), 156	8.261	− 33.6	− 18.8	− 66.5	55.6	− 63.3
		C5-H5A···S1,	2.496(2), 162						
		Cg3···Cg3	3.8332(3)^b						
	1+x,y,z	C8-H8A···O1,	2.497(1), 166	7.492	− 27.7	− 14.5	− 48.7	47.3	− 43.6
		C9-H9A···N3,	2.608(1), 168						
		C18-H18C···S1	2.919(1), 143						
	2-x,2-y,1-z	C17-H17A···O1,	2.676(1), 122	6.416	− 7.0	− 8.4	− 46.3	30.1	− 31.6
		H18···Cg2	2.79^c						
MULMUD	1-x,-y,-z	N1-H1A···S1	2.68(2), 171	6.533	− 68.9	− 42.1	− 49.0	91.8	− 68.2
	2-x,1-y,-z	N2-H2A···O1,	2.34(2), 132	4.415	− 30.3	− 9.8	− 83.2	61.5	− 61.8
		Cg2···Cg3	3.8029(2)^b						
	x,1+y,z	C7-H17···S1	2.882(1), 135	7.422	− 9.9	− 8.9	− 30.9	25.4	− 24.4
	1-x,1-y,-z	C16-F1···Cg2	3.7197(2)	4.088	− 31.5	− 14.4	− 90.4	58.6	− 77.6
MULNAK	2-x,1-y,-z	N1-H1A···S1	2.55(2), 170	6.606	− 72.8	− 47.3	− 44.1	93.7	− 70.5
	1-x,1-y,-z	N2-H2A···O1,	2.68(2), 119	4.459	− 24.0	− 9.2	− 69.7	48.3	− 54.6
		H15···Cg2	2.90^c						
	1.5-x,½+y,-½-z	H4···Cg2	2.90^c	10.617	− 5.0	− 2.8	− 24.1	15.4	− 16.4
XATSET	1-x,2-y,-z	N2-H2···S1	2.56(3), 173	6.472	− 60.1	− 44.2	− 42.8	77.8	− 69.4
	1-x,1-y,1-z	C5-H5B···O1A	2.532(2), 140	5.942	− 23.0	− 8.8	− 55.6	32.1	− 55.3
XATRUI	2-x,1-y,1-z	N2-H2···S1	2.63(3), 175	6.192	− 58.4	− 41.7	− 42.9	76.4	− 66.6
	1-x,1-y,-z	C5-H5B···O1	2.598(2), 143	6.706	− 21.0	− 7.4	− 30.1	18.7	− 39.8
	2-x,1-y,-z	H6A···Cg1	2.77^c	6.467	− 10.7	− 5.4	− 37.4	26.0	− 27.6

*The description of the interaction was modified for better understanding.

fingerprint maps, corresponding to points on the surface where sulphur and oxygen atoms act as acceptors inside the molecular surface, while the N–H (and C–H for AJIQAN, XATSET and XATRUI) groups in a molecule outside the surface act as donors. A complementary spike at the top left region ($d_e > d_i$) represents the reciprocal interactions.

The H···H interactions (labelled 4) is highlighted in the middle of scattered points in 2D-fingerprint maps, with minimum values of ($d_e + d_i$) around 2.2 Å. By the other hand, the short H···H contacts have the most contribution to the total Hirshfeld surface relative to other contacts, varying from 25% in MULNAK to 60% in XATSET (Figure 7), as consequence of the relative abundances of H-atoms in the respective molecules.

3.10. Molecular electrostatic potentials

Two views of the molecular ESP map of title compound are presented in Figure 8, revealing a highly polar molecule ($\mu = 3.63$ D) with a region of strongly negative ESP (−0.065 au) surrounding the S1 atom, and a complementary zone of strongly positive ESP (0.119 au) near the H1 hydrogen atom (Figure 8(a)). These values favour a dominant electrostatic formation of intermolecular N–H···S hydrogen bonds in this structure.

On the opposite side of the surface (Figure 8(b)) involving other pair of adjacent molecules, it is observed an area with lower ESPs value of −0.054 au around the O1 atom, and a zone of 0.073 au around the H2A atom, which indicate intermolecular N1–H2A···O1
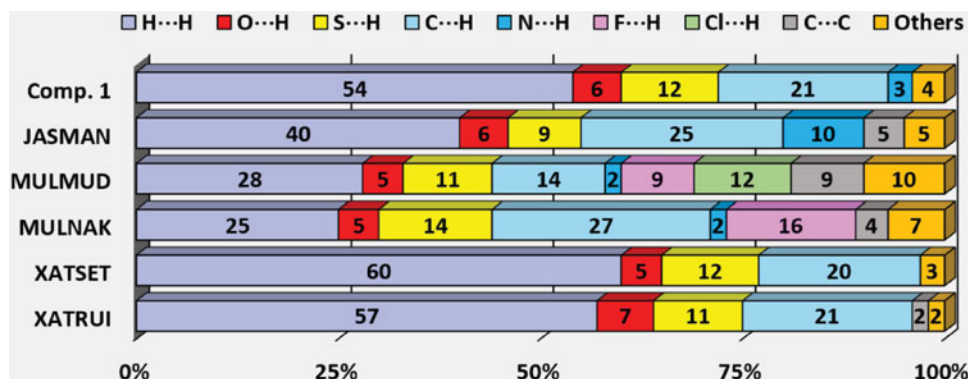

Figure 7. Relative contributions of various intermolecular contacts to the Hirshfeld surface area in **1** and five related structures.
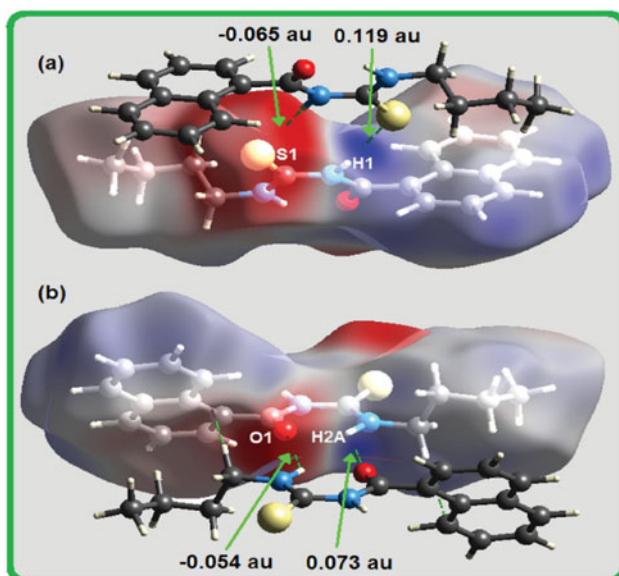
Figure 8. Views of Hirshfeld surface mapped with electrostatic potential over the range ± 0.120 au, in two orientations: (a) front view, (b) back view (180° rotated around the vertical axis of the plot). Intermolecular contacts are shown as dashed lines. The iso-surface is drawn at 0.008 eau^{-3}.

hydrogen bonds electrostatically less favoured. The molecules of four related structures present high polarity in the range 3.89–6.12 D (Table S17, ESI†), and the behaviour of ESPs near the corresponding N–H···S and H···O interactions is similar to those found for title compound, in agreement with energetic results.

4. Conclusions

The new compound has the amide and thioamide functions, connected to each other in a planar conformation and linked by a strong intramolecular C=O···H-N hydrogen bond interaction in both solution and solid state. The most stable calculated conformation is coincident with that found in the crystal, indicating that the intramolecular interactions are possibly more relevant in the adopted conformation than the intermolecular ones. The ^{1}H NMR spectrum shows the naphthyl C9-H as the most deshielded aromatic proton indicating that the C9-H···O interaction persist in non-polar solvent. The AIM approach reveals that this interaction is also present in acetonitrile. The strong stabilisation caused by hyperconjugative interaction from the LPs of the sulphur atom to the LP* of the thiocarbonyl carbon atom constitute almost half of the total stabilisation energy. This fact might explain the decreasing of the bond order and the lengthening of the C–S bond, which was verified by the location of the C–S IR stretching band. The expected

high polarisation of the thioamide group, C12(=S)-N2, could be responsible of the high charge transfer from its nitrogen atom, causing the shortest C- bond length in the molecule, and consequently the shifting of the C–N stretching IR band at higher frequencies.

A complete investigation of intermolecular interactions in the title compound was performed, including a comparison with five closely related structures. Lattice energy determination indicates that the dispersion component has a dominant contribution to the total energy for all compounds. Intermolecular interaction energies of selected molecular dimers indicate maxima contribution (40.5%–47.8%) towards the lattice stabilisation coming from coulombic component only in the case of N–H···S hydrogen bonds. Hirshfeld surfaces give a visual three-dimensional (3D) picture of the nature and proportion of intermolecular interactions in all five structures. 2D-fingerprint plots indicate short H···H contacts as the most contributing interactions (28%–60%) to the total Hirshfeld surfaces. The ESP maps allowed a visual study on the dominant electrostatic nature of intermolecular N–H···S hydrogen bonds in the crystal stabilisation of all structures, supported by Pixel energy values.

In summary, the nature of intermolecular interactions in crystal structures of a series of six naphthoylthiourea derivatives was fully analysed, and it can be useful for the prediction of supramolecular motifs in this type of compounds.

Disclosure statement

No potential conflict of interest was reported by the authors.

References

[1] I.-J. Kang, L.-W. Wang, C.-C. Lee, Y.-C. Lee, Y.-S. Chao, T.-A. Hsu, and J.-H. Chern, Bioorg. Med. Chem. Lett. **19** (7), 1950–1955 (2009).

[2] R. del Campo, J.J. Criado, E. Garcıa, M.a.R. Hermosa, A. Jiménez-Sánchez, J.L. Manzano, E. Monte, E. Rodrıguez-Fernández, and F. Sanz, J. Inorg. Biochem. **89** (1–2), 74–82 (2002).

[3] J. Müller, C. Limban, B. Stadelmann, A.V. Missir, I.C. Chirita, M.C. Chifiriuc, G.M. Nitulescu, and A. Hemphill, Parasitol. Int. **58** (2), 128–135 (2009).

[4] M.K. Rauf, A. Talib, A. Badshah, S. Zaib, K. Shoaib, M. Shahid, U. Flörke, D. Imtiaz ud, and J. Iqbal, Eur. J. Med. Chem. **70**, 487 (2013).

[5] A.C. Tenchiu, M. Iliş, F. Dumitraşcu, A.C. Whitwood, and V. Cîrcu, Polyhedron **27** (18), 3537–3544 (2008).

[6] K.R. Koch, Coord. Chem. Rev. **216** (Supplement C), 473–488 (2001).

[7] F.Z. El Aamrani, A. Kumar, J.L. Cortina, and A.M. Sastre, Anal. Chim. Acta. **382** (1), 205–213 (1999).

[8] M. Domınguez, E. Anticó, L. Beyer, A. Aguirre, S. Garcıa-Granda, and V. Salvadó, Polyhedron **21** (14–15), 1429–1437 (2002).

[9] F.Z. El Aamrani, A. Kumar, L. Beyer, J.L. Cortina, and A.M. Sastre, Hydrometallurgy **50** (3), 315–330 (1998).

[10] E. Scrocco and J. Tomasi, Adv. Quantum Chem. **11**, 115 (1979).

[11] P. Politzer, S.J. Landry, and T. Waernheim, J. Phys. Chem. **86** (24), 4767–4771 (1982).

[12] R.F.W. Bader, Chem. Rev. **91** (5), 893–928 (1991).

[13] F. Jensen, *Introduction to Computational Chemistry* (John Wiley & Sons, Chichester, 2013).

[14] J.D. Dunitz and A. Gavezzotti, Chem. Soc. Rev. **38** (9), 2622–2633 (2009).

[15] A. Gavezzotti, New J. Chem. **40**, 6848–6853 (2016).

[16] S.K. Seth, D. Sarkar, A.D. Jana, and T. Kar, Cryst. Growth Des. **11** (11), 4837–4849 (2011).

[17] S.K. Seth, I. Saha, C. Estarellas, A. Frontera, T. Kar, and S. Mukhopadhyay, Cryst. Growth Des. **11** (7), 3250–3265 (2011).

[18] A. Saeed, M. Bolte, M.F. Erben, and H. Pérez, Cryst. Eng. Comm. **17** (39), 7551–7563 (2015).

[19] M. Owczarek, I. Majerz and R. Jakubas, Cryst. Eng. Comm. **16** (33), 7638–7648 (2014).

[20] K.B. Wiberg and Y. Wang, ARKIVOC **v**, 45–56 (2011).

[21] M.T. Molina, M. Yáñez, O. Mó, R. Notario, and J.L.M. Abboud, in *PATAI'S Chemistry of Functional Groups* (John Wiley & Sons, Ltd, Chinchester, 2009).

[22] K.B. Wiberg, Acc. Chem. Res. **32** (11), 922–929 (1999).

[23] K.B. Wiberg and D.J. Rush, J. Am. Chem. Soc. **123** (9), 2038–2046 (2001).

[24] *CrysAlis PRO* (Oxford Diffraction Ltd, Yarnton, England, 2009).

[25] G. Sheldrick, Acta Crystallogr. Sect. A. **64** (1), 112–122 (2008).

[26] S. Zaib, A. Saeed, K. Stolte, U. Flörke, M. Shahid, and J. Iqbal, Eur. J. Med. Chem. **78**, 140–150 (2014).

[27] S. Miertuš, E. Scrocco, and J. Tomasi, Chem. Phys. **55** (1), 117–129 (1981).

[28] J. Tomasi and M. Persico, Chem. Rev. **94** (7), 2027–2094 (1994).

[29] J. Tomasi, B. Mennucci, and R. Cammi, Chem. Rev. **105** (8), 2999–3094 (2005).

[30] C.J. Cramer and D.G. Truhlar, Acc. Chem. Res. **41** (6), 760–768 (2008).

[31] M. Cossi, N. Rega, G. Scalmani, and V. Barone, J. Comp. Chem. **24** (6), 669–681 (2003).

[32] A.D. Laurent and D. Jacquemin, Int. J. Quantum Chem. **113** (17), 2019–2039 (2013).

[33] E.D. Glendening, J.K. Badenhoop, A.E. Reed, J.E. Carpenter, and F. Weinhold, *NBO 4.0.* (Theoretical Chemistry Institute, University of Wisconsin, Madison, WI, 1996).

[34] F. Biegler-Konig and J. Schonbohm, *AIM 2000 version 2.0.* (University of Applied Science, Bielefeld, 2002).

[35] M.J. Frisch, G.W. Trucks, H.B. Schlegel, G.E. Scuseria, M.A. Robb, J.R. Cheeseman, G. Scalmani, V. Barone, B. Mennucci, G.A. Petersson, H. Nakatsuji, M. Caricato, X. Li, H.P. Hratchian, A.F. Izmaylov, J. Bloino, G. Zheng, J.L. Sonnenberg, M. Hada, M. Ehara, K. Toyota, R. Fukuda, J. Hasegawa, M. Ishida, T. Nakajima, Y. Honda, O. Kitao, H. Nakai, T. Vreven, J.A. Montgomery, J.E. Peralta, F. Ogliaro, M. Bearpark, J.J. Heyd, E. Brothers, K.N. Kudin, V.N. Staroverov, R. Kobayashi, J. Normand, K. Raghavachari, A. Rendell, J.C. Burant, S.S. Iyengar, J. Tomasi, M. Cossi, N. Rega, J.M. Millam, M. Klene, J.E. Knox, J.B. Cross, V. Bakken, C. Adamo, J. Jaramillo, R. Gomperts, R.E. Stratmann, O. Yazyev, A.J. Austin, R. Cammi, C. Pomelli, J.W. Ochterski, R.L. Martin, K. Morokuma, V.G. Zakrzewski, G.A. Voth, P. Salvador, J.J. Dannenberg, S. Dapprich, A.D. Daniels, Farkas, J.B. Foresman, J.V. Ortiz, J. Cioslowski, and D.J. Fox, *Gaussian 09, Revision B.01* (Wallingford, Connecticut (CT), 2009).

[36] S.M. Jasman, W.M. Khairul, T. Tagg, K. KuBulat, R. Rahamathullah, S. Arshad, I.A. Razak, and M.I.M. Tahir, J. Chem. Crystallogr. **45** (7), 338–349 (2015).

[37] A. Saeed, S. Ashraf, J.M. White, D.B. Soria, C.A. Franca, and M.F. Erben, Spectrochim. Acta A **150**, 409 (2015).

[38] S. Ashraf, A. Saeed, M.A. Malik, U. Flörke, M. Bolte, N. Haider, and J. Akhtar, Eur. J. Inorg. Chem. **2014** (3), 533–538 (2014).

[39] A. Gavezzotti, J. Phys. Chem. B **107** (10), 2344–2353 (2003).

[40] A. Gavezzotti, J. Phys. Chem. B **106** (16), 4145–4154 (2002).

[41] J.J. McKinnon, M.A. Spackman, and A.S. Mitchell, Acta Crystallogr. Sect. B-Struct. Sci. **60** (6), 627–668 (2004).

[42] M.A. Spackman, Chem. Rev. **92** (8), 1769–1797 (1992).

[43] J.J. McKinnon, D. Jayatilaka, and M.A. Spackman, Chem. Commun. **43**(37), 3814–3816 (2007).

[44] M.A. Spackman and D. Jayatilaka, Cryst. Eng. Comm. **11** (1), 19–32 (2009).

[45] S. Wolff, D. Grimwood, J. McKinnon, M. Turner, D. Jayatilaka, and M. Spackman, Crystal. Explorer (Version 3.0, University of Western Australia). 2012.

[46] A.S. Mark, Phys. Scripta. **87** (4), 048103 (2013).

[47] D. Jayatilaka, D.J. Grimwood, A. Lee, A. Lemay, A.J. Russel, C. Taylor, S.K. Wolff, P. Cassam-Chenai, and A. Whitton, TONTO – A System for Computational Chemistry. University of Western Australia, 2005.

[48] M.A. Spackman, J.J. McKinnon, and D. Jayatilaka, Cryst. Eng. Comm **10** (4), 377–388 (2008).

[49] G. Tian, Y. Mo, and J. Tao, J. Chem. Phys. **146** (23), 234102 (2017).

[50] J.L. Jios and H. Duddeck, Z. Naturforsch. **55b**, 189 (2000).

[51] R.F.W. Bader and H. Essén, J. Chem. Phys. **80** (5), 1943–1960 (1984).

[52] A.B. Raschi, E. Romano, A.M. Benavente, A.B. Altabef, and M.E. Tuttolomondo, Spectrochim. Acta A **77** (2), 497–505 (2010).

[53] N. Okulik and A.H. Jubert, Int. Electron. J. Mol. Des. **4**, 17–30 (2005).

[54] U. Koch and P.L.A. Popelier, J. Phys. Chem. **99** (24), 9747–9754 (1995).

[55] P.L.A. Popelier, *Atoms in Molecules. An Introduction* (Pearson Education, Harlow, 2000).

[56] R.J. Boyd and S.C. Choi, Chem. Phys. Lett. **120** (1), 80–85 (1985).

[57] R. Custelcean, M.G. Gorbunova, and P.V. Bonnesen, Chem. –Eur. J. **11** (5), 1459–1466 (2005).

[58] M.T. McBride, T.-J.M. Luo and G.T.R. Palmore, Cryst. Growth Des. **1** (1), 39–46 (2001).

[59] R. Custelcean, Chem. Commun. (3), 295–307 (2008).

[60] G.L. Succaw, T.J.R. Weakley, F. Han, and K.M. Doxsee, Cryst. Growth Des. **5** (6), 2288–2298 (2005).

[61] P. Wagner, S. Niemczyk-Baltro, and M. Kubicki, Acta Crystallographica Section C. **59** (2), o83–o84 (2003).

[62] A. Okuniewski, J. Chojnacki, and B. Becker, Acta Crystallogr. Sect. E. **68** (3), o619–o620 (2012).

[63] F. Adam, N. Ameram, and N.E. Eltayeb, Acta Crystallogr. Sect. E. **70** (8), o885 (2014).